Influence of chemical composition and prior microstructure on diode laser hardening of railroad steels

CrossMark

S.M. Shariff [a,*], T.K. Pal [b], G. Padmanabham [a], S.V. Joshi [a]

[a] Center for Laser Processing of Materials, International Advanced Research Center (ARCI) for Powder Metallurgy & New Materials, Hyderabad, India
[b] Department of Metallurgical and Materials Eng., Jadavpur University, Kolkata, India

ARTICLE INFO

ABSTRACT

Diode laser surface treatment of three different railroad steels, namely pearlitic railroad-rail steel (PRS), ferritic–pearlitic railroad-wheel steel (FPRS) and bainitic railroad-rail steel (BRS), has been investigated. Power-ramping experiments, with in-situ surface temperature measurement, were initially carried out to assess surface temperature effects on treated layers. Influence of laser energy on characteristics of treated layers like surface topology, case-depth, microstructure and micro-hardness was comprehensively analyzed. Results revealed that the hardened layer depth is governed by both the process parameters as well as the nature of the substrate steel. With melting, significant reduction in hardness was noted owing to an increase in residual austenite and coarsening of martensitic microstructure. Unlubricated dry-sliding wear tests performed under close to real rail/wheel conditions revealed substantial improvement in wear resistance of hardened/melted rail steels compared to the parent substrates. The observed differences in characteristics of the laser-treated layers and their tribological behavior have been correlated with the chemistry and prior microstructure of the parent substrates.

© 2013 Elsevier B.V. All rights reserved.

1. Introduction

With the ever increasing use of railway networks, steels used in railroads are subjected to increasingly severe operating conditions with accompanying demand for enhanced load carrying capacity, increased speed etc. Various types of railroad steels, ranging from simple pearlitic–ferritic to super-pearlitic and bainitic microstructures, are used depending on the loading conditions and environment [1–3]. As these steels have been already pushed to their limit in terms of hardness improvement and microstructural refinement by adopting various thermo-mechanical treatments during their production, surface modification techniques are being explored for further improving their tribological performance. While mechanical lubrication, boride coating etc. have been found to yield considerable extension of life [4], their practical application on specific contours is complex in terms of labor intensiveness, maintenance requirements and demographic conditions.

Laser surface hardening is a promising technology already implemented in various industrial sectors spanning automotive, power generation and general engineering, but remains yet to be exploited by the railroad industry [5,6]. Laser hardening provides distinct advantages for localized processing of complex areas with precision. High productivity, elimination of post-processing, vast reduction in distortion, no requirement of auxiliary quenching, high process flexibility and maneuverability in industrial environment are additional benefits. Many studies have reported significant improvement in wear resistance of steels of varying chemical composition by employing laser hardening/melting technique utilizing CO_2 and Nd:YAG lasers [7–16]. In a previously reported work by the present authors, improvement in wear resistance of pearlitic railroad rail steel was noted after laser surface hardening/melting utilizing a CO_2 laser [17]. Glassy/nanocrystalline phases resulting due to high cooling rates that prevail in laser processing have been reported to potentially serve as solid state lubricants and mitigate sub-surface cracking in rails, while also being compliant with contacting wheel profiles [18,19].

With the recent advent of compact diode laser sources, reliable and cost-effective processing by mounting the laser on a mobile carrier is also now realistically possible, making it more amenable for treating rails in a railway network. The utility of a diode laser for surface treatment has already been widely reported [20]. Pashby and co-workers have demonstrated the technical feasibility of utilizing diode lasers for hardening both plain carbon and alloy steels [21]. Pantser and Kunjappa have shown that surface hardening of low-alloyed martensitic stainless steels can yield clean polished surfaces, eliminating the need for any post grinding [22]. Present authors have also reported diode laser hardening of various steels used in automotive applications [23–25]. Very recently, Sridhar and co-workers have observed a five to ten-fold increase in sliding wear resistance of plain-carbon and medium-carbon low-alloyed steels as compared to untreated substrates, depending upon the processing conditions adopted [26].

Notwithstanding the above reports, no comparative study on laser hardening of railroad steels with prior pearlitic and bainitic microstructures has been reported. Hence, the present study is aimed at investigating the efficacy of adopting diode-laser surface treatment, by hardening and/or melting, for improving the hardness and wear performance of a variety of railroad steels. Laser surface treatment of three different railroad steels comprising prior microstructures of fully pearlite, pearlite–ferrite and fully bainite was carried out, the treated layers comprehensively characterized and their tribological behavior assessed for improvement in wear performance compared to the parent railroad steels.

2. Experimental procedure

2.1. Railroad steels

Table 1 depicts the chemical composition of the three different railroad steels used in the present study, namely pearlitic railroad steel (PRS), ferritic–pearlitic railroad steel (FPRS) and bainitic railroad steel (BRS). Their microstructures comprised fully pearlite, pearlite with 15–18% ferrite and fully bainite, respectively, as reported in a previous work by the authors [27]. The PRS and FPRS materials constitute popular railroad steels used for rails and wheels by the Indian Railways, while the BRS steel, used in certain railway lines of European and Japanese networks, was acquired from CSIRO Manufacturing and Infrastructure Technology, Australia. Flat plates of 10 mm thickness were EDM cut from the railroad components and ground to 0.5 μm R_a roughness prior to laser treatment to ensure near-identical surface finish on all specimens and to facilitate reliable surface-temperature measurement during laser processing.

2.2. Diode laser surface treatment

Laser surface treatment was carried out employing an integrated fiber-coupled high power diode laser (HPDL) system with a 915–980 nm wavelength beam, tailored to a rectangular beam of size 17 mm × 2 mm with appropriate optics, under an argon shroud. A rectangular nozzle with a 20 mm × 3 mm orifice was utilized for delivering argon gas during processing for shielding to avoid atmospheric contamination. The HPDL system consisted of a diode laser (Laserline GmbH, Germany), capable of delivering a maximum of 6 kW power through a 1.5-mm optical fiber (N.A. 0.22), mounted on the 6th axis of a robot (Reis GmbH & Co Maschinenbau-Fabric GmbH, Germany) integrated to an optical head and an in situ Lampocpro–EMaqs camera system (IWS Fraunhofer, Germany). Fig. 1 shows a view of the set up used for processing. Apart from the shroud gas nozzle, an air-curtain in the form of a cross-jet with high pressure air flow was also used for protecting the focusing lens during processing.

Prior to processing of railroad steel samples, power-ramping experiments were initially conducted for identifying onset of hardening and melting with process conditions summarized in Table 2. For the above experiments, a fixed scan speed of 6 mm/s with ramping of laser power from 500 W to 1600 W in 12 s was employed so that the entire range from "no-hardening" to "substantial melting" was covered. The ratio of laser power (P) to processing speed (V) that corresponds to onset of hardening and melting was determined
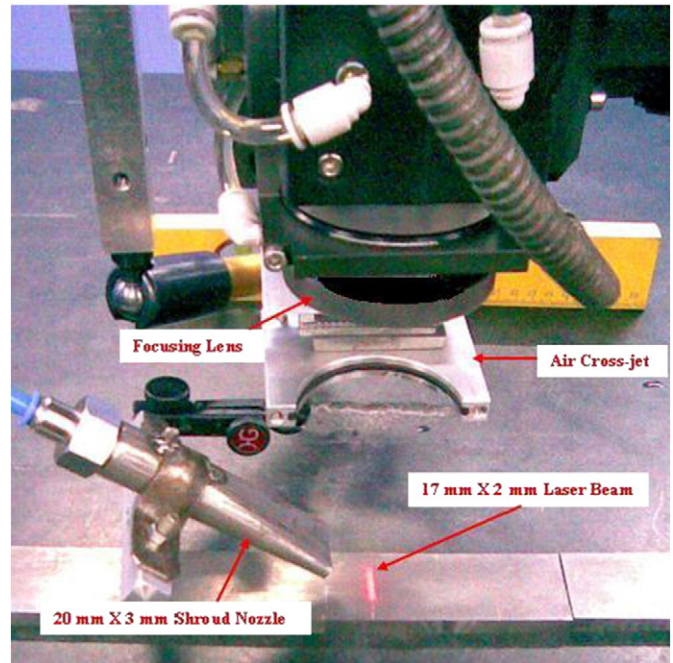

Fig. 1. Laser surface hardening set-up utilized for the study.

from these initial experiments and found to vary within the range of 86–158 J/mm depending upon the type of steel. Subsequently, laser treatment was carried out on all railroad steels with two different P/V values, fixed at 100 J/mm to achieve transformation hardened condition and at 200 J/mm to realize a thin surface melted layer. In the Lastronic-Lampocpro system used for in situ surface temperature measurement, the E-Maqs camera was calibrated for temperature measurement in the range of 800–1300 °C.

2.3. Surface analysis of treated layers

After generation of laser treated tracks on the candidate railroad steels to intentionally achieve different surface modifications (hardened as well as melted), the as-treated surfaces were subjected to topology analysis utilizing a stereo/optical microscope attached with an image-analyzing system (Olympus Corporation, Japan), a scanning electron microscope (Hitachi Inc., Japan) attached with an EDS analyzer utilizing specialized Li-drifted Si detector X-rays (Thermo Electron Corporation, USA) and a 3-D optical surface profilometer (Zygo Corporation, USA). A Mo target with low-speed scanning was utilized for identification of various phases present in as-treated surfaces by X-ray diffraction (Bruker AXS, Germany). Quantitative and qualitative analyses of elemental composition and spatial distribution of elements on the surface were carried out using spot analysis by EDS at various regions of interest in an effort to explain the various morphological features noted in laser-treated layers obtained employing different processing conditions. Utilizing a 3D profilometer having a lateral resolution of 0.37–9.5 μm, surface topographic profiles elucidating various roughness and waviness parameters like R_a (arithmetic mean of surface roughness),

Table 1
Chemical composition of railroad steels used in the study.

Railroad steel	C	Mn	Si	Cr	Ni	Mo	Cu	V	Al	S	P	Fe
PRS	0.67	1.13	0.27	Nil	Nil	Nil	Nil	Nil	<0.01	<0.02	<0.02	Bal.
BRS	0.14	0.76	0.46	2.06	3.07	0.51	1.52	<0.03	0.04	<0.02	<0.03	Bal.
FPRS	0.51	0.74	0.36	0.23	0.19	0.05	0.17	<0.02	Nil	<0.02	<0.02	Bal.

Table 2
Processing conditions employed for identifying hardening and melting regimes in railroad steel utilizing in-situ surface temperature measurement with power-ramping experimentation.

Laser	Fiber coupled diode laser
Workstation	6-Axis robotic system
Laser wavelength	915–980 nm
Fiber	1500-μm (N.A. 0.22)
Surface-temperature measurement system	Lasertronic-Lampocpro 7.6 with E-Maqs (USB)
Laser beam spot (FWHM)	17 mm × 2 mm (rectangular)
Working distance	135 mm
Shroud	Argon at 3 bar
Shroud nozzle stand-off	20 mm × 3 mm orifice with 20 mm stand-off
Scanning speed	6 mm/s
Duration of test	20 s
Laser power	500–1600 W
Sample condition	Ground to 0.5 R_a finish

W_a (arithmetic mean of surface waviness) and PV (maximum distance between highest and lowest peaks), also defined as R_t, were measured at five different locations on the surface and their average values have been reported herein.

2.4. Microstructure and hardness analysis

Comprehensive characterization of microstructure, microhardness and phase constitution was also carried out across the depth of the treated layers utilizing optical microscope, SEM and XRD. For this purpose, as-treated samples were sectioned utilizing a slow-speed saw and metallographic samples were prepared by mounting, grinding and polishing. In case of power-ramping experiments, the entire laser-treated track was first longitudinally sectioned through the center with a slow-speed saw and then the sectioned sample was mounted by employing a resin-based cold mounting method. The mounted specimens were etched with 3%-Nital for pearlitic steels and Vilella's Reagent (a solution comprising 5 ml HCl and 1-g Picric acid in 100 ml Methanol) for BRS to delineate the microstructure. Apart from phase analysis of as-treated surfaces carried out with X-ray diffractometer as explained previously, sub-surface XRD analysis was also carried out on laser-treated layers after the removal of the oxide scale formed in the as-treated surfaces by subjecting to grinding and polishing. Utilizing multi-pattern *Rietveld* method of profile matching and integrated intensity refinement of XRD data utilizing FullProf.2k (V4.80, ILL JRC) software, approximate quantification of various phases was carried out and grain size as well as cell parameters were evaluated in the treated layers. The XRD results obtained were also co-related with the EDS data. An automated Vickers microhardness tester was used for hardness measurement across the depth of the treated layers at 500 gf load.

2.5. Wear testing

Sliding wear tests were carried out using a conventional ball-on-disk tribometer under unlubricated dry conditions to ascertain changes in

Table 3
Ball-on-disk sliding wear testing conditions employed in the study.

Wear test conditions	
Disk material	Laser-treated and untreated PRS, FPRS and BRS steels (ground)
Ball material	5 mm diameter WC ball
Normal load	50 N
Duration of test	0.5 h
Disk rotation speed	200 rpm
Ambient atmosphere	25–32 °C with 60–70% RH
Condition	Dry

the tribological behavior of laser-treated railroad steels in hardened as well as melted conditions and, compared to untreated substrates. A 5-mm diameter tungsten carbide ball, with a hardness of 1800–1900 HV, was used for sliding against as-received and laser-treated specimen disks of 20-mm diameter. The conditions adopted for sliding wear testing are similar to that reported in an earlier study by the same authors, which ensured that the Hertzian contact pressures during sliding were close to actual rail/wheel contact conditions [27]. The tribometer was capable of applying a controlled normal load in the range of 0.1–100 N as well as simultaneously monitoring and recording the tangential frictional force, normal load, and sliding speed during testing. All wear experiments were carried out at least three times and the average results have been reported herein. The wear testing conditions mentioned in Table 3 were found to yield 2.1 GPa Hertzian contact pressure, which is comparable to the contact pressure in actual wheel/rail conditions. At the end of the wear test, the volume wear loss of each tested disk was calculated from the wear trough area measured using a surface profilometer [28]. From the measured volume loss, specific wear rate, K, was evaluated by using the relationship defined in a previously reported study [29].

3. Results and discussions

3.1. Power-ramping experiments to identify processing windows for transformation hardening and melting

Fig. 2 depicts a longitudinally sectioned macrostructure of the entire laser treated track obtained during power-ramping experiments carried out on all three railroad steels (PRS, FPRS and BRS) used in the study. The aim of these preliminary experiments was to identify the values of power density, defined as the ratio of laser power (P) to scan speed (V), that correspond to onset of surface hardening as well as surface melting in case of each of the railroad steels investigated. It is clear that the chemical composition and prior microstructure influence the hardening/melting of a railroad steel. Although laser processing was carried out under argon shielding, the tendency of oxygen to react with a steel increases with temperature. XRD analysis of the treated surfaces reported later clearly confirmed formation of oxides on treated surfaces, despite employing neutral gas shielding as has also been reported in previous studies [30,31]. The type of oxide layer formed and its rate of growth, however, are expected to depend on the alloying elements present in the steel and the ambient conditions associated with the process that possibly influence heat transfer characteristics. As a consequence of the variations in the chemistry of the steels and their thermophysical properties, differences were observed in the power levels corresponding to onset of hardening and onset of melting in case of the three steels studied.

The onset of hardening can be clearly distinguished from the variation in microstructure of hardened region as compared to that of parent substrate. The laser power levels at which onset of hardening was noted were 545 W, 565 W and 520 W for PRS, FPRS and BRS, respectively. Similarly, laser powers corresponding to onset of melting (attainment of solidus temperatures) could also be clearly identified (marked in the cross-sectional micrographs) and were observed to be 935 W, 950 W and 700 W for PRS, FPRS and BRS respectively. The solidus temperatures corresponding to onset of melting were measured to be PRS, FPRS and BRS were 1240 °C, 1255 °C and 1130 °C, respectively. Significant reduction in solidus temperature of BRS could be attributed to presence of alloying elements such as Cr, Ni, Mo and Cu in steel. From Fig. 2, it is clear that minimum laser power levels of 520 W (corresponding to a P/V value of 86.67 J/mm) and 700 W (corresponding to a P/V value of 116.67 J/mm) were required for hardening and melting of BRS steel. In case of PRS and FPRS, somewhat higher P/V values were noted for onset of hardening (90.8 J/mm for PRS, 94.2 J/mm for FPRS) and onset of melting (155.8 J/mm for PRS, 158.3 J/mm for FPRS). In view of the above results, the P/V ratio was varied between
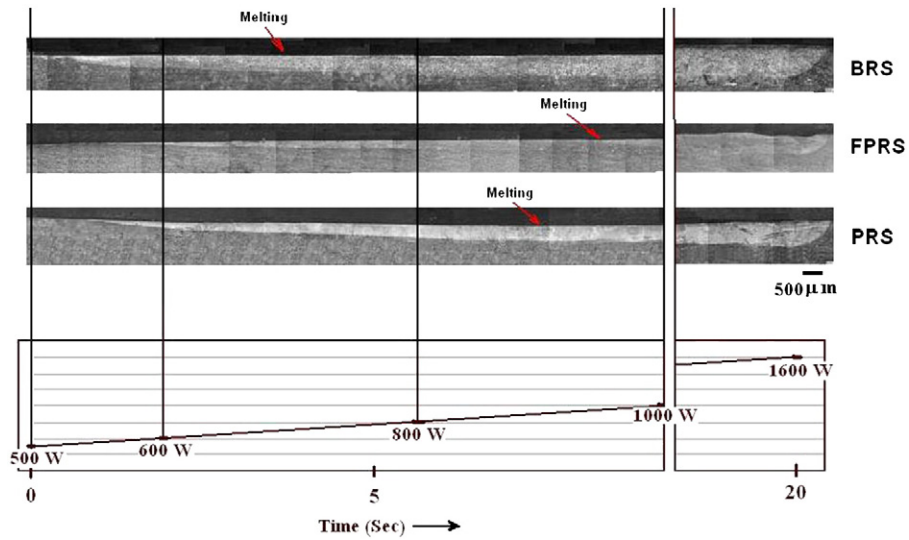
Fig. 2. Cross-sectional macrographs along with laser power measurements made during power-ramping experiments conducted on railroad steels with a scan speed of 6 mm/s. The onset of melting is marked in case of each steel substrate.
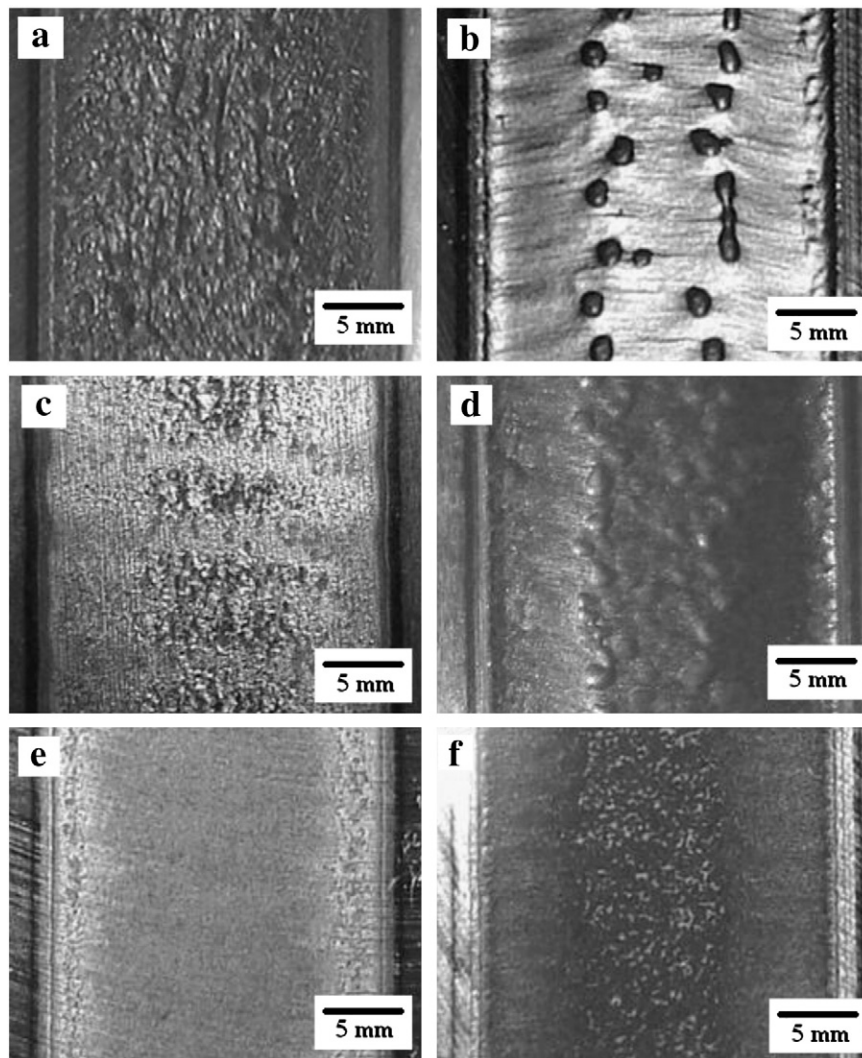

Fig. 3. Surface morphologies of laser-treated layers processed under different conditions: (a) PRS-hardened, (b) PRS-melted, (c) FPRS-hardened, (d) FPRS-melted, (e) BRS-hardened and (f) BRS-melted.

100 J/mm and 200 J/mm for further experimentation to ensure that the range covered conditions of full transformation hardening (without any trace of melting) as well as shallow melting on all the steels investigated.

3.2. Surface morphology of laser treated surfaces

Fig. 3 illustrates low magnification surface morphologies of as-treated railroad steels processed under two conditions, specifically those corresponding to P/V = 100 J/mm and P/V = 200 J/mm, which ensured transformation hardening and melting conditions. The laser treated track width in case of hardening was noted to be marginally higher in BRS (17.3 mm) as compared to PRS (16.9 mm) and FPRS (16.8 mm), plausibly due to prior bainitic microstructure and its higher thermal diffusivity [13,29]. In a similar study involving CO_2 laser hardening of tempered AISI 4150 steel, a wider and deeper case was observed in steel with prior bainitic microstructure compared to a pearlitic one [8]. The surfaces of laser hardened FPRS and BRS appeared more yellowish and smoother than in case of PRS, suggesting formation of different oxides. The presence of scattered fine and bright ribbles, particularly in hardened layers of PRS and FPRS, could be associated with formation of fragile iron oxide particulates. The melted surfaces additionally revealed formation of globules/droplets possibly due to protrusions/undulations associated with the combined effect of melt-pool driven convection currents and oxidation. However, these features were found to be much less in BRS compared to PRS or FPRS.

Fig. 4 illustrates the topographic profiles as well as surface roughness parameters of laser-treated and untreated steel surfaces obtained with a 3D profilometer. It is clear from the topographic pictures that there is only a marginal increase in the average roughness (R_a) and average waviness (W_a) values in case of hardened surfaces, with disappearance of unidirectional grinding furrows. However, the PV values (alternatively R_t, a measure of maximum distance between highest and lowest peaks in the measured roughness profile) increased substantially to 22–42 μm and 24–38 μm, respectively, in hardened surfaces of PRS and FPRS, compared to the corresponding starting values of 4.2–6.8 μm and 4.1–7.2 μm. In contrast, the PV values in case of hardened BRS underwent very little change. This is consistent with the surface morphologies of hardened surfaces previously shown in Fig. 3. The relatively lower PV values in case of BRS could be attributed to the formation of a regular smooth oxide film constituting chromium oxide, as explained later. Surface topographic profiles (Fig. 4(g–i)) with high PV values clearly indicate the presence of heavy undulations on melted surfaces in case of all railroad steels. Similar surface roughness effects were reported in other prior studies involving laser melting of steel and attributed to material removal, re-solidification and oxidation/phase transformation effects, depending on the parameters involved [32,33]. Indeed, the topographic dimensions of these undulations (like PV values) on the melted surfaces depend on material transformation and evaporation effects under the heat input conditions involved in the process [34].

3.3. Phase constitution and elemental–composition analysis of laser treated surfaces

Fig. 5 depicts the XRD patterns of untreated and laser processed steels, while SEM morphologies with elemental distribution as
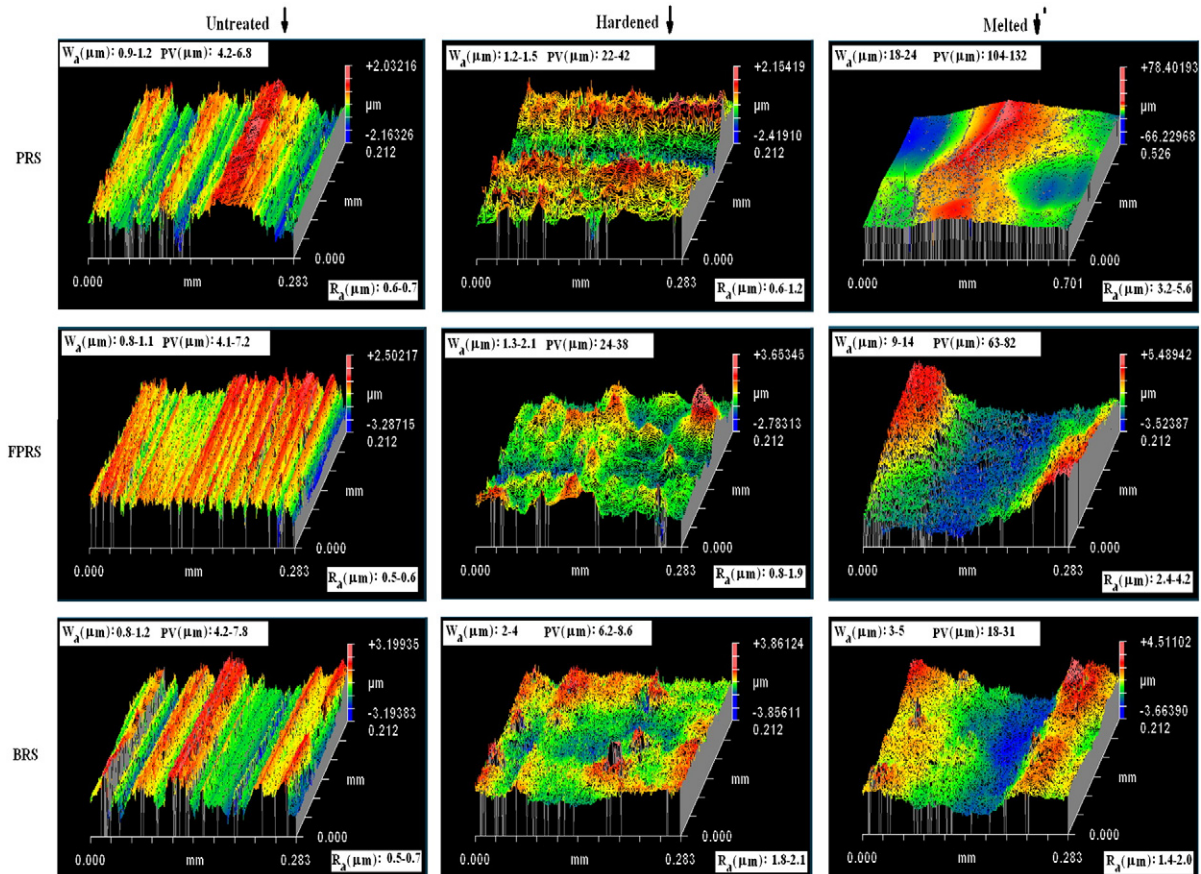

Fig. 4. Surface profiles of untreated railroad steels as well as those laser-treated layers processed under different conditions.
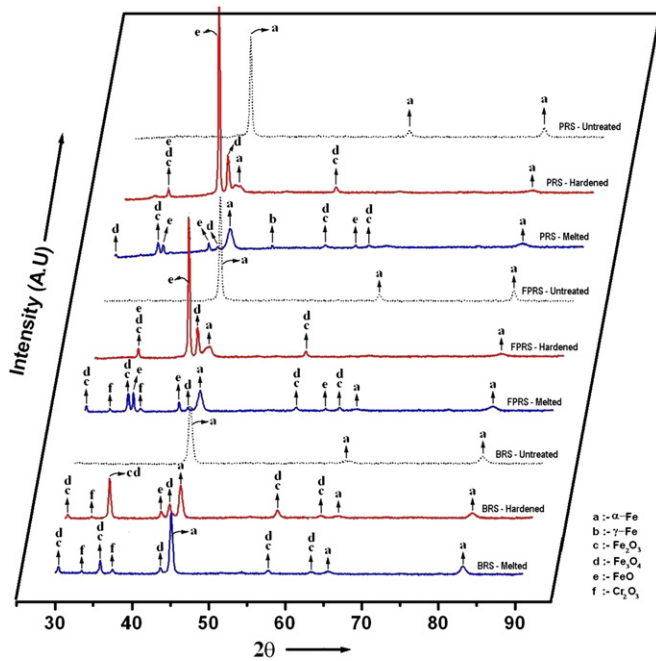
Fig. 5. XRD patterns of untreated and laser-processed railroad steel surfaces.

determined by EDS analysis are depicted in Fig. 6 to gain further understanding of laser-treated surface characteristics and assess the effect of steel chemistry and prior microstructure. It is clear that, under processing conditions that lead to transformation hardening, the presence of α-Fe is reduced as compared to oxide products in case of all steels. Hardened surfaces of all steels were found to comprise predominantly of oxides of iron (FeO, Fe_2O_3 and Fe_3O_4) as compared to oxide-free untreated parent substrates, although the quantum and relative presence of different oxides varied depending on the steel involved. Previously, many studies on laser hardening of steels have also reported formation of such oxides, despite processing under inert gas shielding, possibly on account of the propensity for oxidation at high temperatures that typically result during laser processing [22,30]. The melted surface with undulations is bright and shiny when compared to the hardened surface as observed in Fig. 3(b) in case of PRS.

Hardened/melted surfaces of FPRS and BRS appeared yellowish and dull as compared to PRS, possibly due to different oxide layers formed on treated surfaces of the steels due to the presence of alloying elements such as Cr, Ni etc. In a similar study involving laser hardening of AISI 420L steel, yellowish surface appearance has been reported on account of formation of chromium oxides on the treated surface [22]. Indeed, the presence of chromium oxide (Cr_2O_3) peaks in XRD patterns of hardened BRS and melted BRS/FPRS surfaces appears to corroborate this aspect. As Cr and Ni contents are less in FPRS compared to BRS, chromium oxide peak could not be observed in hardened FPRS. As oxidation reaction temperature for chromium is higher than that for iron [30], the amount of chromium oxide on the surface of hardened layers is lower than that of melted ones. Indeed, Cr_2O_3 peak could not be detected at all in hardened FPRS.

The morphologies of laser-treated surfaces were also different on account of different oxides formed on the treated layers, as evident from the high magnification SEM micrographs depicted in Fig. 6. The surfaces of hardened layers of FPRS and BRS are relatively smooth and with regular oxide film formation as compared to that noted in PRS. This suggests that the presence of alloying elements in steel, such as Cr, Ni etc., facilitates formation of a regular adherent oxide film. Furthermore, higher Cr and Ni contents in BRS facilitated the formation of chromium oxide as observed in the XRD pattern. Melting also facilitated substantial oxidation of Cr and, as a result, a somewhat different surface morphology with islands showing higher chromium and oxygen content (as per EDS spot analysis in region 12 of Fig. 6(f)) could be observed in BRS. Indeed, the XRD analysis also showed higher amount of Cr_2O_3 in the melted surface of BRS than on the transformation hardened surface.

3.4. Microstructure analysis

A detailed microstructural analysis of treated layers was carried out after removing the oxide film by polishing and then analyzing their cross-sections. Figs. 7 and 8 depict the cross-sectional macrostructures and the near-surface microstructures of treated layers of all railroad steels under hardened and melted conditions. In Fig. 7, the various regions with distinct microstructures across the affected cross-section have been delineated by appropriate etching and have been marked as MZ (melted zone), HZ (transformation hardened zone) and TZ (transition zone wherein partial austenetization is involved). The total case depths (constituting MZ, HZ and TZ) for PRS, FPRS and BRS were noted to be 385 ± 10 μm, 405 ± 15 μm, and 615 ± 20 μm, respectively, in layers processed with P/V = 100 J/mm. The case depths increased to 840 ± 10 μm, 860 ± 18 μm and 1120 ± 25 μm in melted layers processed with P/V = 200 J/mm as a direct consequence of the enhanced heat input. Under similar processing conditions, the case depths in PRS and FPRS were largely similar, whereas BRS showed a much deeper case depth. The deeper hardening effect in BRS could be attributed to the shorter carbon diffusion distances in a prior bainitic microstructure as compared to that in a pearlitic microstructure [9].

The substantial depth of the TZ region (about 140 μm) with partially transformed microstructure in case of FPRS could be attributed to the wider gap in critical austenetization temperatures, i.e., AC_1 and AC_3, associated with the steel. Thus, initial microstructure associated with prior treatment and critical transformation temperatures (AC_1, AC_3, T_M and M_s) determine the microstructural transformations in treated steels. Indeed, the enhanced depth of HZ regions in PRS and BRS (by 25%) than FPRS could be due to the substantial reduction in carbon-diffusion distances associated with their prior microstructures constituting uniformly distributed pearlite and bainite. In a similar study involving laser hardening of tempered 4340 steel, fine and more evenly distributed carbides in prior microstructure were found to yield deeper hardened depths owing to vast reduction in carbon-diffusion distances [9].

The near-surface melted layer of BRS (depicted in Fig. 8(i)) showed a distinctly dendritic microstructure, plausibly due to the significant presence of Cr and Ni in BRS, whereas no such dendrites could be observed in PRS and FPRS. Indeed, the comparative XRD analysis of Fe $(200)_\alpha$ peak from untreated and laser processed surfaces depicted in Fig. 9, provides some insight into the formation of phases in laser treated layers. The significant shift in Fe$(200)_\alpha$ peak towards lower 2-theta values, as evident from the XRD patterns, is indicative of hardening effect. The high cooling rate associated with laser treatment process could have contributed to such a martensitic transformation. Similar observations showing peak shift on account of melting or hardening have been reported in a laser hardening study on cast iron by Roy and Manna [35]. However, the amount of martensite, residual austenite and carbides, along with their sizes and morphologies in treated layer, is quite different in each case. Further high magnification SEM microstructures, with qualitative EDS spectral analysis at select regions of the treated layers, was also carried out and is presented in Figs. 10–11 to provide further insight into the microstructural variations associated with laser processing.

The chemical composition and prior microstructure influence the critical austenetization temperatures (AC_1 and AC_3), the solidus temperature (T_M) and the martensite start temperature (M_s) that play a
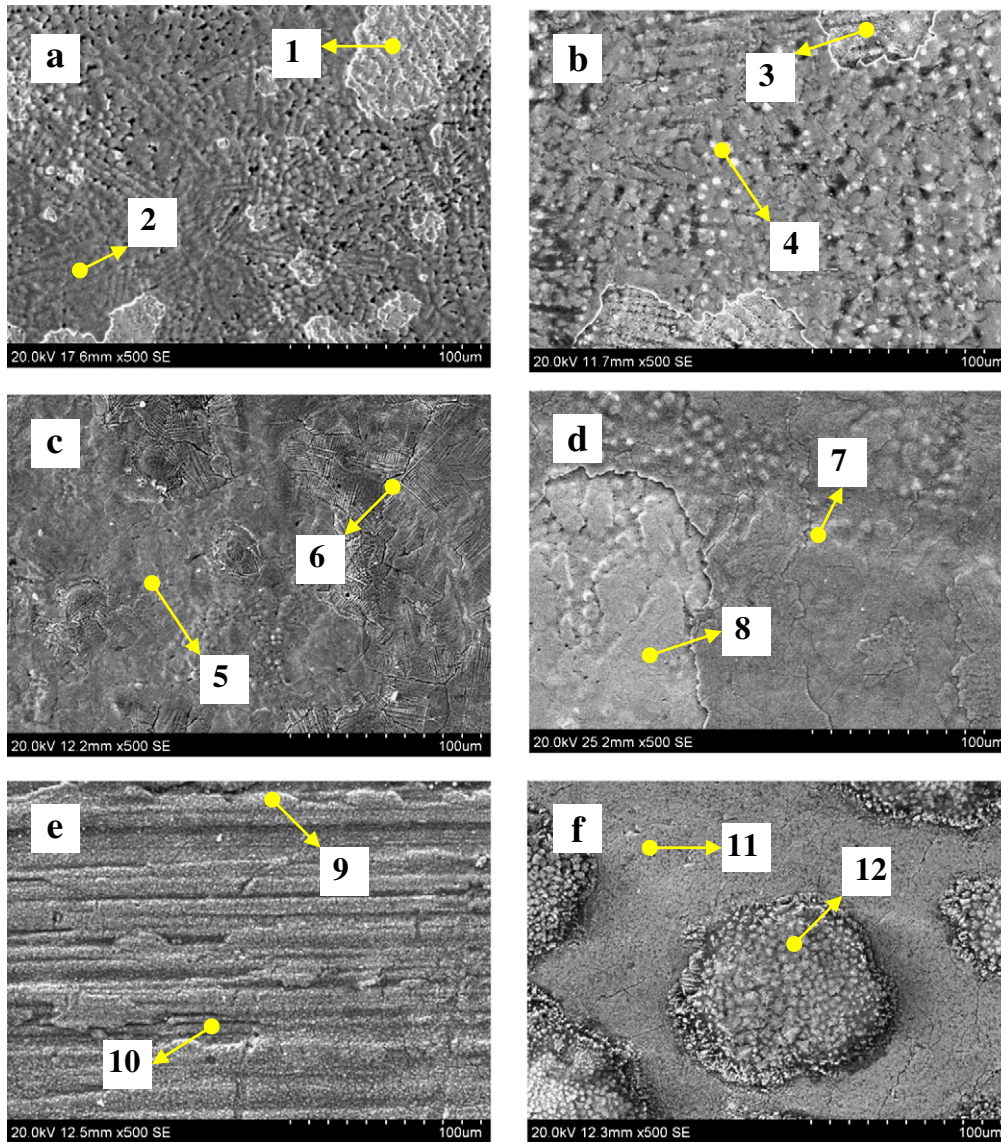
Region	O	Mn	Si	Fe	Cr	Ni
1	0.3	0.1	0.2	96.8	-	-
2	9.4	0.5	0.1	88.2	-	-
3	0.7	1.3	0.1	93.4	-	-
4	16.2	4.1	1.2	75.4	-	-
5	13.8	3.5	0.8	82.1	0.1	0.0
6	15.2	8.7	3.1	71.7	0.2	0.0
7	14.8	0.7	0.2	74.8	0.1	0.0
8	0.2	0.2	0.1	92.2	0.1	0.1
9	15.8	8.9	3.2	68.4	4.8	0.6
10	14.6	0.9	0.6	72.8	1.2	2.7
11	13.8	1.2	0.8	72.4	2.1	1.6
12	23.6	11.3	12.6	27.6	17.4	0.1

Fig. 6. SEM surface morphologies and EDS analysis of laser-treated layers processed under different conditions: (a) PRS-hardened, (b) PRS-melted, (c) FPRS-hardened, (d) FPRS-melted, (e) BRS-hardened and (f) BRS-melted.
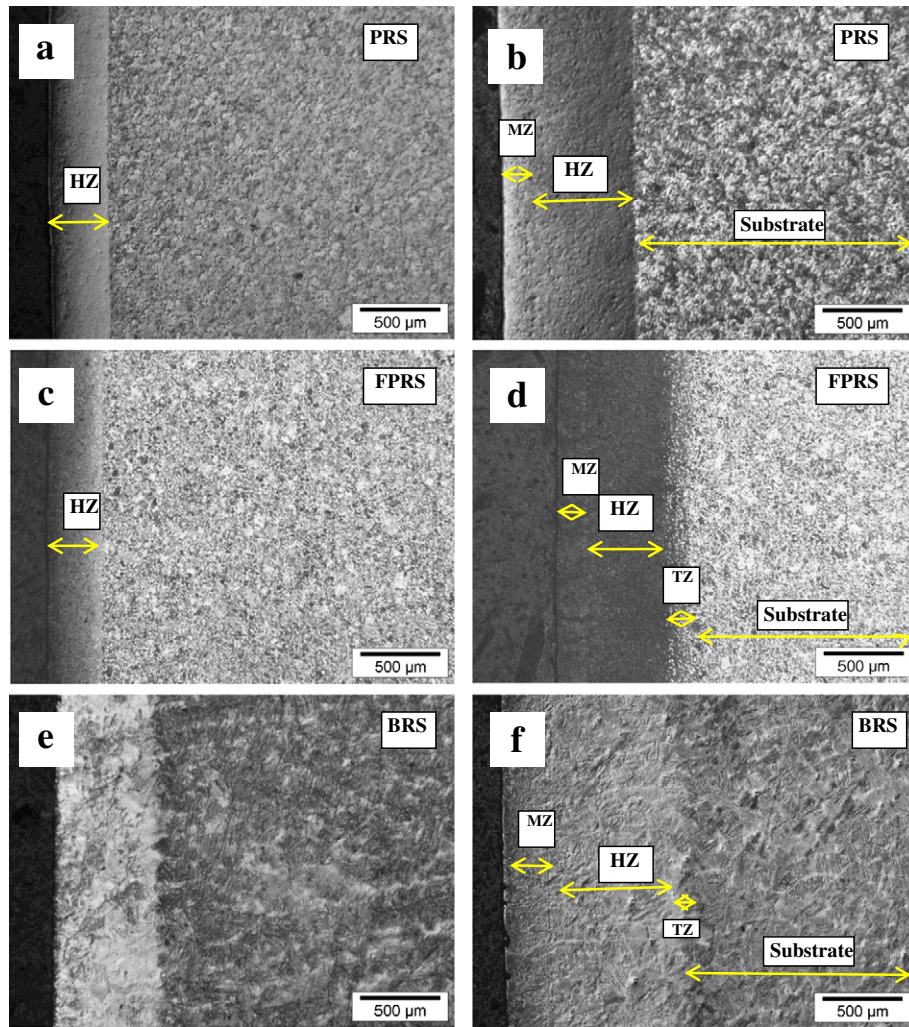
Fig. 7. Cross-sectional optical micrographs of railroad steels processed under different conditions: (a) PRS-hardened, (b) PRS-melted, (c) FPRS-hardened, (d) FPRS-melted, (e) BRS-hardened and (f) BRS-melted.

pivotal role in determining the final transformed microstructures that are obtained after laser treatment. Generally, the peak surface temperature should be restricted to just below T_M to obtain fully transformation hardened case with maximum hardness. Raising the surface temperature significantly beyond T_M results in melting, leading to adverse effects like high amounts of residual austenite, induced tensile stresses, loss of important alloying elements and sometimes cracking. Restricting the input laser energy to 200 J/mm ensured melting of only a thin surface layer without any presence of cracks. The transformation hardened regions (HZ) of PRS and FPRS below MZ, depicted in Fig. 10(b & d), indicated microstructures comprising fine plate-type martensite with coarse prior austenite grains (grayish sheaves) and few carbides (bright spots) in PRS and a mix of plate and lathe-type martensites with fine austenite grains in FPRS, respectively. Melted regions of PRS and FPRS depicted in Fig. 10(a and c) exhibited more or less similar microstructures with coarse martensite, large prior austenite grains, few iron oxides (2–5 μm) and ultrafine pores (1–2 μm). Enhanced diffusion of oxygen at high temperatures, coupled with melt pool turbulence, could have contributed to the presence of ultrafine pores and iron oxides in melted layers. In a similar study involving laser melting of steels, Carbucicchio and Palombarini detected iron oxides in the melt region by XRD and Mossbauer analyses [11]. Indeed, the qualitative EDS spectral analysis of these particulates,

indicating high oxygen content in few black spots as compared to that of oxygen-free non-oxide gray region of microstructure depicted in Fig. 10, corroborates these findings.

The amount of residual austenite (R_γ) was also found to be significantly higher in the melted zone (MZ) compared to the hardened and transition zones (HZ/TZ). The amount of residual austenite as per Rietveld analysis of XRD patterns shown in Fig. 9 was found to be 4–6% and 7–10% in MZ of PRS and FPRS, as compared to 2–3% and 4–6% in HZ of PRS and FPRS. The approximate calculation utilizing Rietveld analysis of XRD patterns indicated 2–3 μm sized martensite needles, 5–10 μm sized prior austenite grains (grayish sheaves) and 2–5 μm sized dispersed carbides (cementite) in HZ of PRS as against 1–3 μm sized mixed martensite needles (lathe and plate types) and fine prior-austenite grains (3–6 μm) with no significant presence of dispersed carbides in HZ of FPRS. Similar microstructures have been observed in various other reported studies involving laser hardening of medium carbon and high carbon steels [14,36]. Low carbon diffusion distances (on account of low inter-lamellar ferrite/carbide spacing) in PRS facilitate in high austenitic homogenization during heating cycle, thereby leading to high-stress twinned martensite formation. Indeed, the martensitic cell parameter of 2.884 Å evaluated from the XRD pattern corroborates the high stressed condition in PRS as compared to the cell parameter of 2.867 Å obtained in FPRS martensitic cell.
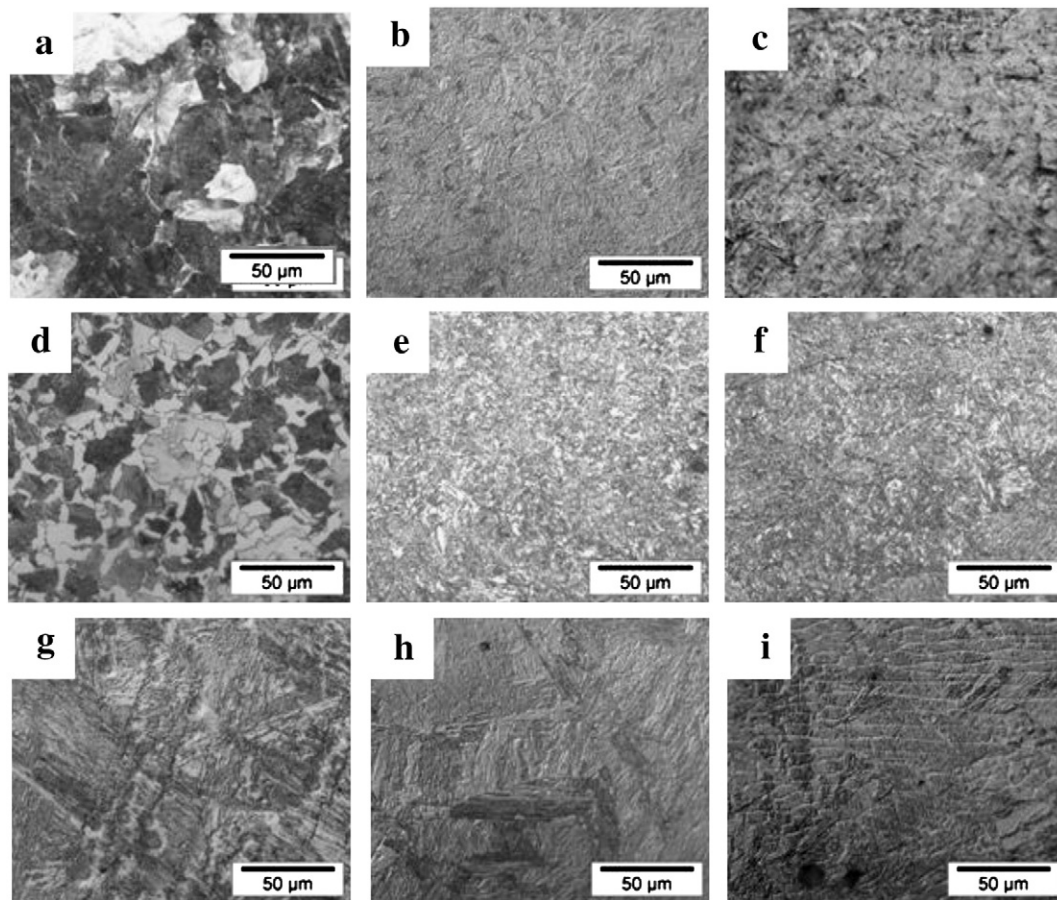
Fig. 8. Cross-sectional optical microstructures of railroad steels processed under different conditions: (a) PRS-untreated, (b) PRS-hardened, (c) PRS-melted, (d) FPRS-untreated, (e) FPRS-hardened, (f) FPRS-melted, (g) BRS-untreated, (h) BRS-hardened and (i) BRS-melted.

The high magnification TZ microstructure near the hardened layer/substrate interface depicted in Fig. 10(e) for laser treated FPRS is distinguishably different from that of the unaffected substrate depicted in Fig. 10(f). The microstructure is a duplex one, comprising martensite and pockets of pro-eutectoid ferrite. In the TZ region, the temperature experienced is between upper and lower critical austenetization temperatures (A_{C3} and A_{C1}) and, hence, rapid carbon diffusion within pearlite colonies (marked in Fig. 10(f)) becomes easier for austenetization during the heating cycle and its subsequent transformation into martensite during the cooling period. In due course, the presence of large islands of pro-eutectoid ferrite (marked in Fig. 10(e)) in FPRS delays diffusion of carbon from ferrite to austenite (due to low temperatures) and thereby no martensitic transformation happens, resulting in the original pro-eutectoid ferrite being retained. Such microstructures in TZ regions were also found in PRS, but the thickness of this region was low (20–30 μm) for it to be significant. Similar transformation in microstructures of transition zones was also reported in various studies involving laser hardening of low and medium carbon steels [9,10].

Fig. 11 depicts the SEM micrographs within the various zones of laser treated BRS processed with 200 J/mm laser energy input. The parent BRS microstructure depicted in Fig. 11(d) indicates a mix of upper and lower bainites (bainitic sheaves interconnected at austenite/martensite boundaries) with fine dispersed carbides. The microstructure in the MZ region, depicted in Fig. 11(a), shows an interdendritic network of composite carbides (like (Fe, M)$_{23}$ C$_6$)) in a coarse cellular/dendritic martensitic matrix. Indeed, comparative qualitative EDS spectral analysis at two different spots in the dendritic and interdendritic regions depicted in Fig. 11 indicate that the interdendritic network is richer in chromium

than dendrites of martensite and, hence, composite carbides of Fe and Cr can be anticipated. Earlier studies involving laser melting of alloy steels have also reported the presence of complex composite carbides of $(Fe, M)_X$ C [12–14]. In fact, in a similar study involving laser alloying of Ni–Cr in steel, formation of such complex carbides as $(Fe, Cr)_{23} C_6$ was also concluded utilizing EDX spectral analysis [16]. Few iron oxide particulates, ultrafine pores were also found to be present in the MZ region as observed in pearlitic railroad steels and can be attributed to oxidation and intense melt-pool turbulences.

Microstructure of hardened region (HZ) of BRS, below MZ, depicted in Fig. 11(b), indicated coarse martensite lathes with disappearance of composite carbide network (as observed in MZ) indicating plausibly complete dissolution of carbides. Indeed, XRD patterns (Fig. 9) indicated substantial Fe$(200)_\alpha$ peak shifting with enhanced intensity in hardened and melted regions of BRS as compared to the untreated parent substrate. The high cooling rates associated with laser hardening did facilitate in martensitic transformation in BRS, although with large prior austenite grains. Similar coarse martensitic microstructure in hardened region, although with more prior bainite, was reported in a study conducted by Fang and Co-workers involving air-cooling of U20Si bainitic steel [37]. As alloy carbides tend to retard cooling rates, the microstructure in BRS plausibly results in coarsening of low-carbon martensite accompanied with solid-solution strengthening of austenite. At a certain depth, close to interface, in TZ region, microstructure (depicted in Fig 11(c)) showed substantial precipitation and coarsening of carbides with prior bainite that could be associated with incomplete austenetization during heating cycle and auto-tempering effect. In a similar study involving laser melting of hardened and tempered 20CrMoV steel, at certain depth of hardened region,
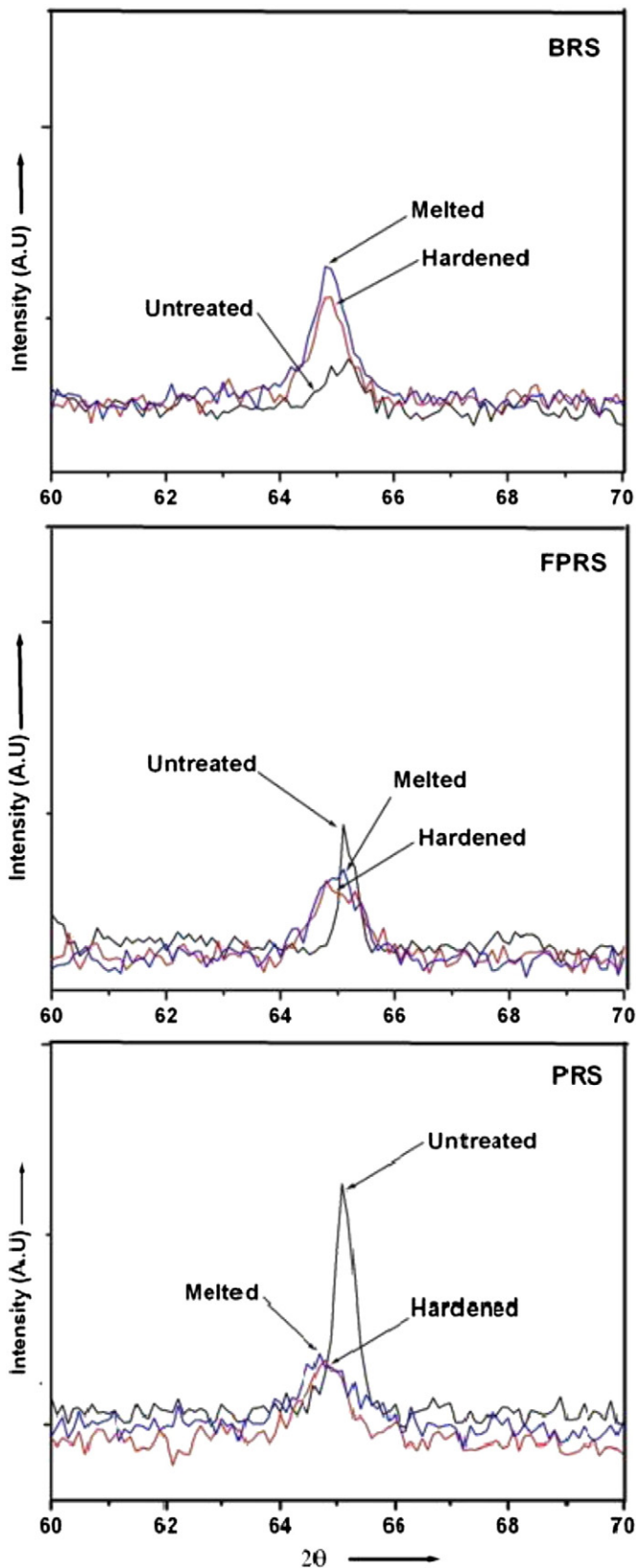
Fig. 9. X-ray diffraction patterns of Fe $(200)_\alpha$ obtained in untreated and laser-processed railroad steels after removal of oxide layer.

dissolution of carbides stopped with coarsening of cementite particles in the microstructure and thereby leading to self annealing or tempering effect [14].

3.5. Hardness distribution in treated layers

Fig. 12 illustrates microhardness profiles obtained across the depth of laser treated layers processed under different conditions. The hardness distribution in various zones (MZ, HZ, TZ and Substrate) of a laser treated FPRS processed at 200 J/mm has been marked in the figure for illustration. Vast improvement in hardness (600–820 HV) due to martensitic transformations discussed previously is noted in PRS and FPRS compared to BRS. The HZ region of BRS exhibited marginal improvement in hardness (440–510 HV), possibly due to coarse low-carbon martensite transformation and solid solution strengthened austenite (with alloy carbides and dislocations). Near surface melted regions obtained in all three laser treated layers processed with 200 J/mm exhibited low hardness as compared to the hardened regions as a consequence with increase in residual austenite and microstructural coarsening effects [17]. In a similar study involving laser melting of plastic mold steel, the marginal improvement in hardness was attributed to solid solution strengthened austenitic microstructure associated with high process cooling rate [15]. Melting of BRS resulted in hardness reduction below that of the parent substrate, possibly due to precipitation of composite carbide network of Fe and Cr and loss of carbon/hardening elements in matrix. However, at certain depth in TZ, close to interface, microhardness value dropped below that of parent steel indicating an auto-tempering effect as discussed previously. In a similar study involving laser hardening of quenched low-carbon alloy steel, carbides precipitated due to self-annealing effect at a certain depth exhibited lower hardness than that of unaffected substrate [14]. In fact, heavy coarsening of microstructure with loss of carbon and alloy carbides with soft martensite/austenite dendrites may lead to substantial hardness reduction in the near surface melted region of BRS processed with 200-J/mm energy input.

3.6. Sliding wear performance

An attempt has been made to study and compare the sliding wear performance of railroad steels processed under different conditions leading to hardening and thin surface melting, with parent substrates by evaluating specific wear rate (k) during unlubricated ball-on-disk wear testing. The volume loss was measured from worn profiles and the average specific wear rate (K) calculated as per procedures explained in the previously reported work by the same authors [27]. Fig. 13 depicting the average specific wear rates (K) clearly shows that layers processed at low P/V value of 100 J/mm leading only to hardening exhibited eight-to-ten-fold lower values when compared with untreated parent pearlitic steels (PRS and FPRS). The marginal reduction in wear resistance of melted layers of PRS and FPRS, in comparison with hardened counterparts, could be due to reduced hardness microstructures. Various previous studies have also reported similar effects of improvement in wear resistance of laser-melted layers of carbon steel and attributed to hardness obtained in their microstructures [12,38].

Despite low hardness improvement in hardened BRS, the wear rate reduced significantly, indicating influence of other factors on wear resistance. Even in melted BRS steel, a 5-fold reduction in wear rate could be observed despite the hardness being as low as 320–380 HV. Solid solution strengthened martensite/austenite with alloying elements of Cr, Mn, Mo etc. may possibly play a decisive role in improving wear resistance. In a similar study involving laser hardening of alloy steels, high wear resistance was observed on account of solid-solution strengthened martensitic microstructures with the presence of Cr and Mo [26]. In fact, few studies have reported improved wear resistance of bainitic steels subjected to laser hardening with principal reason being attributed to martensite transformation [38,39]. On the whole, hard microstructure comprising refined martensitic matrix (with higher carbon content) contributed to the
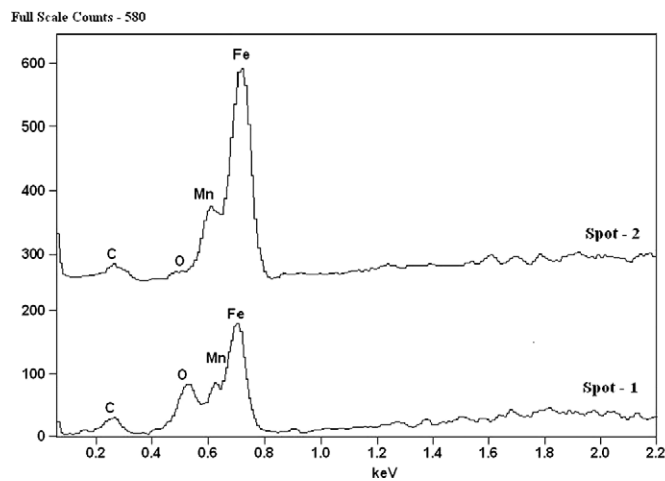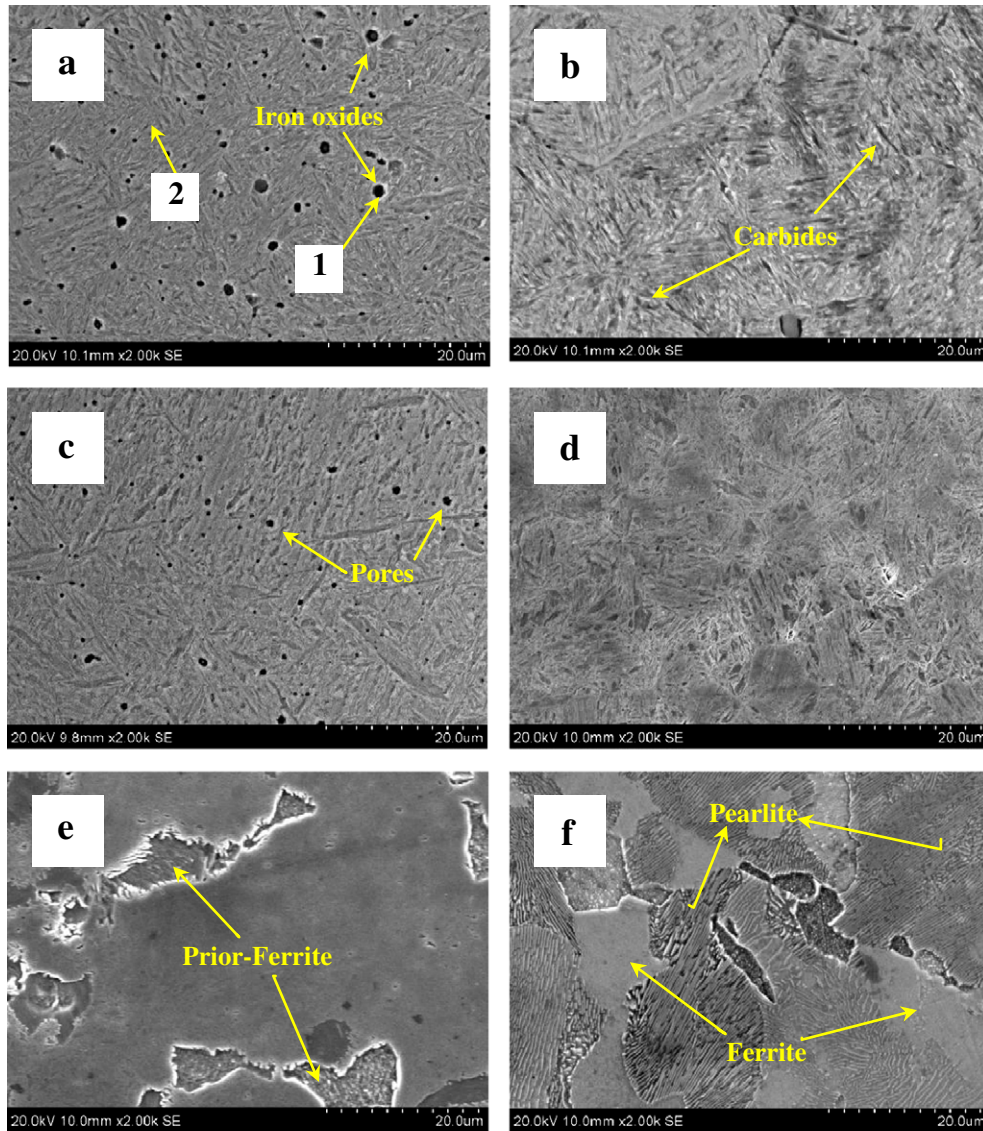
Fig. 10. SEM microstructures of PRS and FPRS at various regions within the treated layer processed with P/V = 200 J/mm: (a) PRS-MZ region, (b) PRS-HZ region below MZ, (c) FPRS-MZ region, (d) FPRS-HZ region below MZ, (e) FPRS-TZ region at hardened/substrate interface, and (f) FPRS unaffected substrate. The qualitative EDS spectral analysis from two different locations marked in the melted microstructure of PRS is also shown below the micrographs.

highest improvement in wear resistance of PRS and soft microstructure comprising coarse solid-solution strengthened martensite/austenite with composite carbides assisted in marginal improvement in wear

resistance of BRS. Thus, the above noted trend is consistent with the hardness profiles previously discussed, with higher hardness values directly leading to enhanced wear resistance.
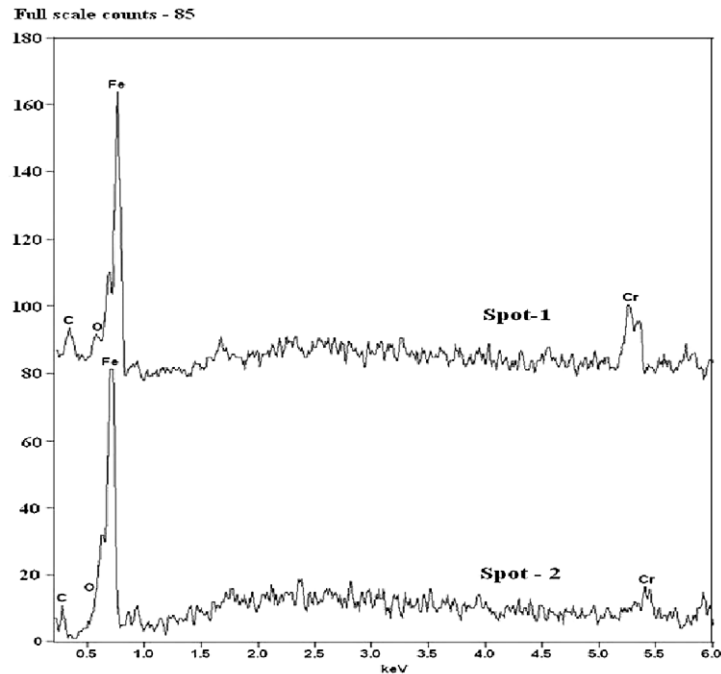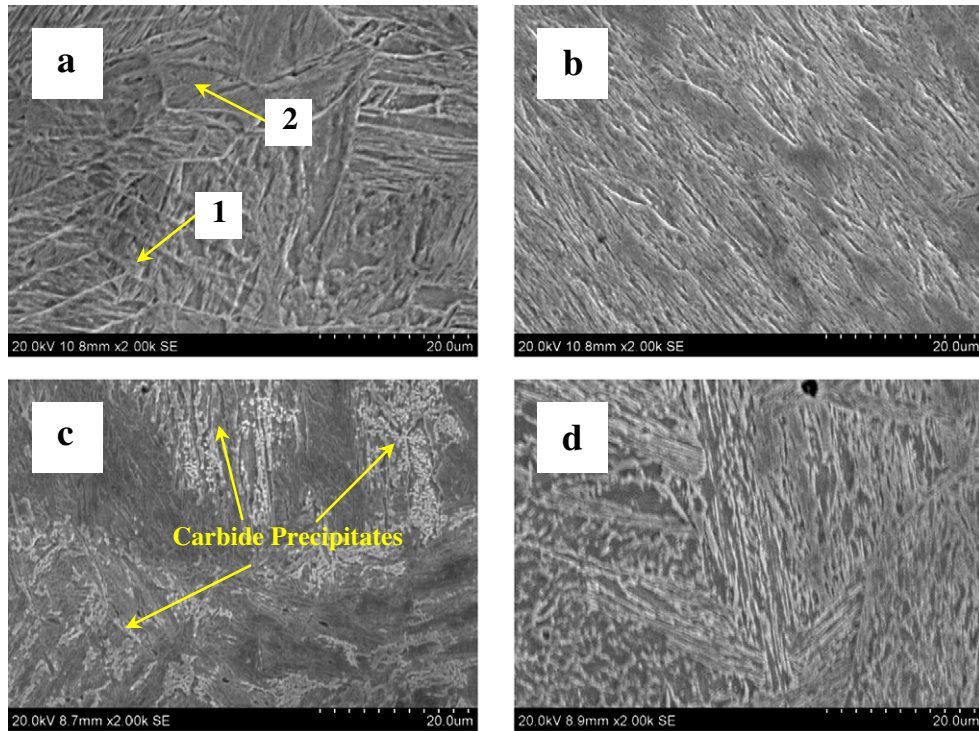
Fig. 11. SEM microstructures of BRS processed under melted condition with P/V = 200 J/mm: (a) MZ region, (b) HZ region below MZ, (c) TZ (softened) region near hardened layer/substrate interface, and (d) unaffected substrate. The qualitative EDS spectral analysis from two different locations (dendritic and inter-dendritic regions) marked in the melted microstructure of BRS is also shown below the micrographs.

4. Conclusions

The present study deals with diode laser processing of three different typically used railroad steels and the comprehensive investigation of laser-treated layers processed under varying conditions leads to the following conclusions:

1. Power ramping experiments enable identification of processing windows for transformation hardening as well as for obtaining crack-free surface melting.

2. Case depth of the treated layer was governed by the laser-energy and chemistry/prior-microstructure of the railroad steel and when processed at similar conditions; it increased in the order of FPRS, PRS and BRS.

3. Surfaces of hardened layers were found to comprise predominantly iron oxides, although, the quantum and relative presence of different oxides varied depending on the railroad steel involved.

4. Presence of Cr and Ni in BRS facilitated smoother laser-treated surfaces as a consequence of adherent continuous chromium oxide film formation.
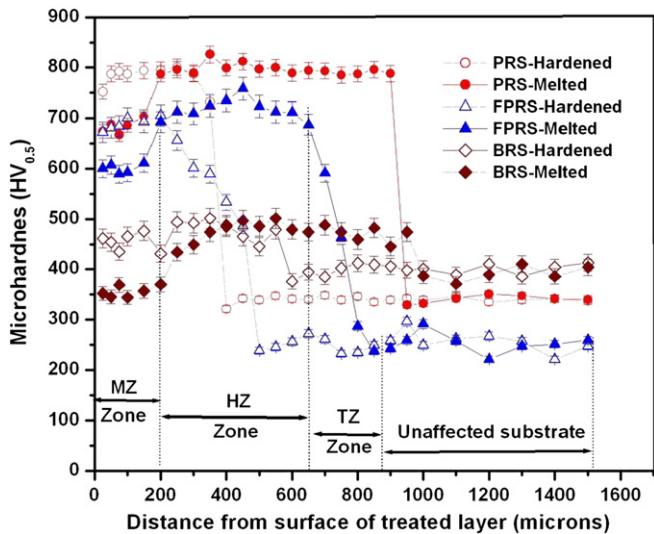
Fig. 12. Cross-sectional hardness profiles across the depth of treated layers of railroad steels processed under different conditions (various zones of interest within the treated layer shown in case of FPRS-melted for illustration purpose).
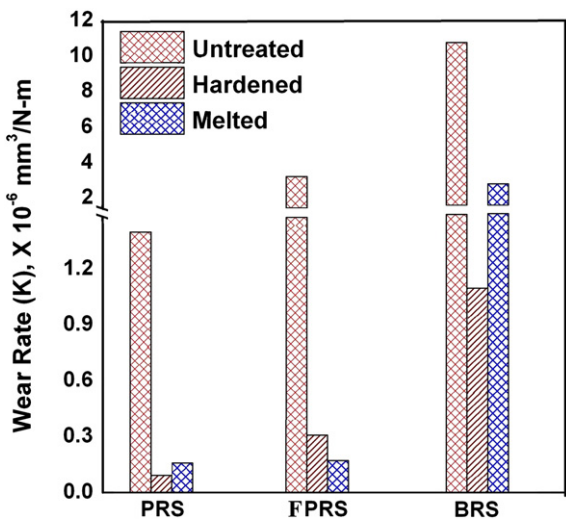

Fig. 13. Comparison of sliding wear behavior of laser-treated railroad steels.

5. Hardened zone microstructure in all steels predominantly comprised of martensite, although their morphologies, amount and size were found to be different in each case. Microstructure in melted zone showed presence of few ultrafine pores and oxides with increase in residual austenite.

6. Significant hardness (600–820 HV) improvement associated with refined martensitic transformations could be observed in PRS and FPRS as against marginal hardness (440–510 HV) improvement in BRS associated with coarse martensitic transformations and prior bainite.

7. Hardened/melted PRS and FPRS showed eight-to-ten-fold improvement in sliding wear resistance as against five-to-seven-fold improvement in hardened/melted BRS when compared with their respective parent substrates.

References

[1] J. Pacyna, J. Achie, Mater. Manuf. 28 (1) (2008) 19.
[2] Mingru Zhang, Jianqing Qian, Haicheng Gu, J. Mater. Eng. Per. 16 (5) (2007) 635.
[3] Peter Pointner, Wear 265 (2008) 1373.
[4] H. Muster, H. Schmedders, K. Wick, H. Pradier, Wear 191 (1996) 54.
[5] In: W.M. Steen (Ed.), Laser Materials Processing, Springer Verlag, New York, 1991.
[6] Laser Institute of America, Handbook of Laser Materials Processing, Magnolia Publishing Inc., 2001
[7] You Wang, Tingquan Lei, Jiajun Liu, Wear 231 (1999) 12.
[8] C. Chen, Chinese J. Mater. Sci. 18 (A2) (1986) 70.
[9] R.K. Shiue, C. Chen, Metall. Trans. A. 23A (1992) 163.
[10] D.I. Pantelis, E. Bouyiouri, N. Kouloumbi, P. Vassiliou, A. Koutsomichalis, Surf. Coat. Technol. 298 (2002) 125.
[11] M. Carbucicchio, G. Palombarini, Thin Solid Films 126 (1985) 293.
[12] S. Kac, J. Kusi'nski, Surf. Coat. Technol. 180-181 (2004) 611.
[13] Henrikki Pantsar, J. Mater. Process. Technol. 189 (2007) 435.
[14] K. Obergfell, V. Schulze, O. Vohringer, Mater. Sci. Eng. A355 (2003) 348.
[15] C.T. Kwok, K.I. Leong, F.T. Cheng, H.C. Man, Mater. Sci. Eng. A357 (2003) 94.
[16] Q. Li, D. Zhang, T. Lei, C. Chen, W. Chen, Surf. Coat. Technol. 137 (2001) 122.
[17] S.M. Shariff, T.K. Pal, G. Padmanbham, S.V. Joshi, Surf. Eng. 26 (3) (2010) 199.
[18] R.J. DiMelfi, P.G. Sanders, B. hunter, J.A. Eastman, K.J. Sawley, K.H. Leong, J.M. Kramer, Surf. Coat. Technol. 106 (1998) 30.
[19] S. Aldajah, O. Ajayi, G.R. Fenske, S. Kumar, J. Tribol. 125 (2003) 643.
[20] E. Kennedy, G. byrne, D.N. Collins, J. Mater. Process. Technol. 155-156 (2004) 1855.
[21] I.R. Pashby, S. Barnes, B.G. Bryden, J. Mater. Process. Technol. 139 (2003) 585.
[22] Henrikki Pantser, Veli Kujanppaa, Surf. Coat. Technol. 200 (2006) 2627.
[23] S.M. Shariff, Manish Tak, G. Padmanabham, N. Gowrishankar, Proc. International Conference on "Automotive Materials & Manufacturing -2010" Pune, India 6–8 October, 2010, p. 143.
[24] B. Syed, A. Halder, S.M. Shariff, G. Padmanabham, I. Manna, Proc. International Conference on "Automotive Materials & Manufacturing -2010" Pune, India 6–8 October, 2010, p. 105.
[25] S.M. Shariff, Manish Tak, S. Shanmugam, G. Padmanabham, Proc. International Mobility Engineering Congress & Exposition — 2009, Chennai, India 13–15 December, SAE International, SAE-2009-28-0053, 2009.
[26] K. Sridhar, V.A. Katkar, P.K. Singh, J.M. Haake, Surf. Eng. 23 (2) (2007) 129.
[27] S.M. Shariff, T.K. Pal, G. Padmanabham, S.V. Joshi, J. Tribology 133 (2011) 1–9, (021602).
[28] Meng Hua, Xicheng Wei, Jian Li, Wear 265 (2008) 799.
[29] You Wang, Tingquan Lei, Jiajun Liu, Wear 231 (1999) 1.
[30] A.C. Agudelo, J.R. Gancedo, J.F. Marco, M.F. Creus, E. Gallego-Lluesma, J. Desimoni, R.C. mercader, Appl. Surf. Sci. 14 (8) (1999) 171.
[31] Chengyun Cui, Hu. Jiandong, Yuhua Liu, Kun Gao, Zuoxing Guo, Appl. Surf. Sci. 254 (2008) 6537.
[32] M. Hua, Se Dao, T.M. Shao, H.Y. Tam, J. Mater. Process. Technol. 192-193 (2007) 89.
[33] Meng Hua, Tianmin Shao, Yuan Tam Hong, Edmund Cheung Hon Man, Surf. Coat. Technol. 185 (2004) 127.
[34] T.M. Shao, M. Hua, H.Y. Tam, E.H.M. Cheung, Surf. Coat. Technol. 197 (2005) 77.
[35] A. Roy, I. Manna, Mater. Sci. Eng. A297 (2001) 85.
[36] F. Lusquin~os, J.C. Conde, S. Bonss, A. Riveiro, F. Quintero, R. Comesan~a, J. Pou, Appl. Surf. Sci. 254 (2007) 948.
[37] Fang Hong-sheng, Feng Chun, Zheng Yan-kang, Yang Zhi-gang, Bai Bing-zhe, J. Iron and Steel Res. Int. 15 (6) (2008) 1.
[38] A. Basu, J. Chakraborthy, S.M. Shariff, G. Padmnabham, S.V. Joshi, G. Sundararajan, J. Dutta Majumdar, I. Manna, Scripta Materalia 56 (2007) 887.
[39] G. Zhang, Q. Yang, Y. Wu, B. Su, 3rd Inter. Cong. s, Maney, London, UK, 1983, p. 9.